RESEARCH ARTICLE

NANO · MICRO small
www.small-journal.com

A Granular Hydrogel-Enabled Wearable Electrochemical Biosensing Platform for Continuous Non-Invasive Sweat Lactate Detection

Farnaz Lorestani, Xianzhe Zhang, Zaman Ataie, Alexander Kedzierski, Yushen Liu, Aarón López, Ankan Dutta, Kyle Kacala, Zhenyuan Niu, Amir Sheikhi,* and Huanyu Cheng**

Although continuous and non-invasive measurements of sweat biomarkers may provide vital health information, sweat collection often involves intense physical activities or chemical/thermal stimuli. The natural body sweat during endogenous metabolic or stress processes, secreted at much lower rates at rest, may be continuously analyzed using microfluidic devices integrated with hydrophilic rigid fillers; however, the sweat uptake and accumulation in thermoregulatory processes take too long for near-real-time measurements. This work provides an innovative body fluid collection strategy using a granular hydrogel scaffold (GHS), facilitating osmotic and capillary effects to uptake and transfer an ultralow amount of sweat into a microfluidic device at rest. Taken together with a spiral microfluidic channel, the GHS-embedded microfluidics reduce the evaporation of collected sweat and store it in a sensing well for near-real-time measurements. Integrating the sweat-collecting system with an enzymatic gold-graphene nanocomposite-modified laser-induced graphene (LIG) electrode and a LIG-based pH sensor enables the accurate continuous on-body detection of sweat lactate during normal daily activities at a low perspiration rate. The novel combination of a GHS-integrated microfluidic system with a low-cost, flexible, sensitive, and stable LIG-based sensing system provides an accessible technology for sweat-based biosensing during normal daily activities.

1. Introduction

Non-invasive wearable sweat sensing systems provide a means for near-real-time monitoring of metabolites[1–4] and other critical biomarkers[5] to analyze sports performance and monitor/manage various health conditions. Compared to other biofluids such as saliva,[6] tears,[7] and urine,[8] sweat offers continuous and on-demand accessibility. However, collecting sufficient sweat for analysis under low-perspiration conditions, such as rest or light physical activities, remains a significant challenge. Human sweating rates under these conditions range from 10 to 100 nL min^{-1} cm^{-2} and vary across body locations and individuals.[9,10] While it is desirable to continuously collect sweat at rest for the near-real-time monitoring of thermoregulatory sweat biomarkers, most wearable sweat sensors only work at high sweat rates, generated from intense physical activities or chemical/thermal stimuli.[11–18] Devices using absorbent materials, such

F. Lorestani, X. Zhang, Y. Liu, A. López, A. Dutta, K. Kacala, Z. Niu, H. Cheng
Department of Engineering Science and Mechanics
The Pennsylvania State University
University Park, PA 16802, USA
E-mail: fkl5072@psu.edu; huanyu.cheng@psu.edu

Z. Ataie, A. Sheikhi
Department of Chemical Engineering
The Pennsylvania State University
University Park, PA 16802, USA
E-mail: sheikhi@psu.edu

The ORCID identification number(s) for the author(s) of this article can be found under https://doi.org/10.1002/smll.202502655

DOI: 10.1002/smll.202502655

A. Kedzierski, A. Sheikhi, H. Cheng
Department of Biomedical Engineering
The Pennsylvania State University
University Park, PA 16802, USA

A. López
Department of Biomedical Engineering and Science
Tecnun Universidad de Navarra
San Sebastian 20018, Spain

A. Dutta
Center for Neural Engineering
The Pennsylvania State University
University Park, PA 16802, USA

A. Sheikhi
Department of Chemistry
The Pennsylvania State University
University Park, PA 16802, USA

as a filter paper, show improved collection during exercise in the range of 1–3 μL min^{-1} cm^{-2},[19] but they are ineffective during low-physical activities and can suffer from delayed wetting, sweat mixing, evaporation, and analyte loss, ultimately compromising continuous monitoring.[16,19,20]

Efforts aimed at tackling the sweat-collection challenge have focused on hydrogels either as standalone layers or integrated into the microfluidic reservoirs to passively draw sweat via osmotic and capillary effects.[21–26] Simultaneously, capillary action enables sweat transport into channels or pores.[27–29] Traditional polymeric hydrogels, such as poly(2-hydroxyethyl methacrylate) (pHEMA) and polyacrylamide,[1,30,31] primarily rely on crosslinked network structures and the interactions between the polymer matrix and water to maintain their water absorbability. However, the absence of capillary channels in these hydrogels results in a low water transport rate (1.2–12 μL h^{-1}).[1] Although sweat uptake has been enhanced by leveraging osmotic and capillary effects in hydrogel-based microfluidic devices, most still require substantial initial sweat volumes to avoid drawback effects, rendering them unsuitable under low-sweating conditions.[26,32–37] Recent strategies have incorporated rigid SU-8 components coated with polyvinyl alcohol and thin agarose-glycerol hydrogel layers in contact with the skin, enabling an uptake rate of 100 nL min^{-1} cm^{-2}.[38] However, these designs may lack material compatibility, leading to delamination, cracking, sweat entrapment, and limited flexibility, along with increased fabrication complexity and cost.[39–46]

Compared with bulk, non-porous hydrogels, porous granular hydrogel scaffolds (GHS), fabricated via the jamming and covalently interlinking of hydrogel microparticles (microgels), may address these challenges. Mathematical models and simulations of the capillary effects in porous media indicate a significant role of liquid density, contact angle, surface tension, and pore characteristics in fluid transport.[47] Therefore, the capillary rise in GHS may be tailored by adjusting the size,[48] shape,[49] packing density,[50] microgel surface properties, and absorbate characteristics.

Beyond sweat collection, accurate biosensing at low analyte concentrations remains challenging, as conventional enzyme-based sensors may have limited durability due to enzyme degradation or poor immobilization. These issues are particularly pronounced at low sweating rates, where biomarkers are less diluted and more physiologically relevant. Various strategies, such as the use of redox mediators, e.g., Prussian blue, crosslinkers, e.g., glutaraldehyde, and stabilizing agents, e.g., Nafion, chitosan, and bovine serum albumin (BSA), have been used to improve immobilization, but have compromised performance parameters.[51–53] Therefore, there is a growing need for scalable, cost-effective, and sensitive wearable platforms capable of detecting biomarkers at ultralow concentrations. Since the sweat pH is in the range from 5 to 7,[54,55] depending on the activity and environment, it may affect sensor accuracy. Thus, monitoring pH is also essential for proper sensor calibration.[56,57]

This work presents a novel integrated flexible, wearable, sensitive, and low-cost sweat sensing platform, equipped with porous GHS in a microfluidic patch for the near-real-time analysis of sweat during non-intensive daily physical activities. We hypothesize that the porous medium in GHS increases absorption capacity compared with non-porous bulk hydrogel counterparts, primarily because of the micron-sized void spaces that enable capillary-driven fluid uptake. Additionally, the sensing performance is improved by modifying a porous laser-induced graphene (LIG) electrode with a reduced graphene oxide-gold nanoparticle (rGO–AuNP) nanocomposite and optimizing enzyme immobilization. This synergistic design enhances sensitivity, stability, and reproducibility at low cost, enabling continuous detection of biomarkers even under low-sweat conditions. By enabling the analysis of physiological states and medical conditions, this platform may contribute to non-invasive, scalable, and cost-effective approaches in personalized medicine, with broader implications for population health.

2. Experimental Section

2.1. Chemicals

The following materials were purchased from Sigma–Aldrich and used without modification: chitosan (50,000–190,000 Da (based on viscosity)), gold(III) chloride hydrate ($HAuCl_4 \cdot xH_2O$, 99.995% trace metals basis), iron(III) chloride ($FeCl_3$, reagent grade, 97%), potassium hexacyanoferrate(III) ($K_3Fe(CN)_6$, ACS reagent, ≥99.0%), Pluronic F-127 (powder, BioReagent, suitable for cell culture), polyvinyl butyral (PVB) (powder), nitric acid (HNO_3, 98%), aniline (ACS reagent, ≥99.5%), calcium chloride ($CaCl_2$, anhydrous, powder, ≥97%), magnesium chloride ($MgCl_2$, anhydrous, ≥98%), sulfuric acid (H_2SO_4, 98%), potassium permanganate ($KMnO_4$, 99.9%), multiwall carbon nanotubes (diameter = 30–50 nm and length = 15 μm) with >95% purity (MWCNT), potassium chloride (KCl, ACS reagent, ≥99.0%), sodium chloride (NaCl, ACS reagent, ≥99.0%), L-lactic acid ($C_3H_6O_3$, meets analytical specification of Ph. Eur. (European Pharmacopoeia), BP, 88%–92% total acid basis), potassium phosphate monobasic (KH_2PO_4, powder, suitable for cell culture, suitable for insect cell culture, suitable for plant cell culture, ≥99.0%), potassium phosphate dibasic (K_2HPO_4, ACS reagent, ≥98%), acetic acid (CH_3COOH, HPLC, Meets ACS Specifications, ≥99.7%), ascorbic acid ($C_6H_8O_6$, reagent grade, crystalline), D-glucose ($C_6H_{12}O_6$, ≥99.5% (GC)), ethanol (C_2H_6O, absolute for analysis EMSURE ACS, ISO, Reag. Ph. Eur.), methanol (CH_3OH, ACS reagent, ≥99.8%), glutaraldehyde ((Glu), $C_5H_8O_2$, Grade II, 25% in H_2O), glycerol ($C_3H_8O_3$, BioXtra, ≥99% (GC)), BSA (lyophilized powder, crystallized, ≥98.0%, BSA), Gelatin Type A from porcine skin (≈300 g Bloom), methacrylic anhydride (contains 2,000 ppm topanol A as inhibitor, 94% purity), Dulbecco's phosphate-buffered saline (DPBS), lithium phenyl-2,4,6-trimethylbenzoylphosphinate (LAP, purity 97%), fluorescein isothiocyanate-dextran (FITC-Dextran) with an average molecular weight of 2 MDa, and Nafion. Food dye (Nomeca, 14

A. Sheikhi
Huck Institutes of the Life Sciences
The Pennsylvania State University
University Park, PA 16802, USA
A. Sheikhi
Department of Neurosurgery
College of Medicine
The Pennsylvania State University
Hershey, PA 17033, USA

Food Coloring Set) was purchased from Amazon. Graphite flakes were procured from Ashbury Inc. pH buffer solutions were purchased from Fisher Chemical. Hydrochloric acid (HCl) was purchased from EMD Millipore Corporation. Milli-Q water purification system (electrical resistivity ≈18 MΩ cm at 25 °C) was provided by Millipore Corporation. Commercial silver (Ag) nanoparticle ink was obtained from NovaCentrix. Polyimide (PI) tapes with a thickness of 50 µm and polydimethylsiloxane (PDMS; Sylgard 184) were purchased from Myjor and The Dow Chemical Company, respectively. Polymethyl methacrylate (PMMA, thickness = 1/12 inch) was purchased from MELOVE Home Deco, China. L-lactate oxidase (LOx) was purchased from Toyobo Corp. Dimethylsiloxane-(60%–70% ethylene oxide) block copolymer (PEG-PDMS block copolymer (BCP)) was obtained from Gelest Inc. Novec 7500 Engineered Fluid was provided by 3 M. PicoSurf (5 vol.% in Novec 7500) was procured from Sphere Fluidics, and 1H,1H,2H,2H-perfluoro-1-octanol (PFO, purity 98%) was supplied by Alfa Aesar. All chemicals were used without further purification.

2.2. Preparation of LIG Nanocomposites and an Enzymatic Lactate Sensor

2.2.1. Synthesis of Reduced Graphene Oxide (rGO) and rGO-AuNPs Nanocomposite

rGO was produced using an adapted version of Hummers' method.[58] To remove the excess acids and salts, the prepared rGO suspension with a concentration of 0.05 wt.% underwent dialysis for 6 h. Subsequently, the dialyzed rGO suspension was centrifuged at 3000 rpm for 20 min to remove the remaining unexfoliated rGO and then dried at 50 °C for 24 h. rGO suspension was prepared by dispersing 1 mg mL^{-1} rGO in deionized (DI) water with 1 h sonication. rGO:AuNPs solution was prepared by mixing the rGO and 0.1 M $HAuCl_4$ solution in three different volume ratios (1:1, 3:1, and 6:1 v/v) with 1 h sonication. Next, a chitosan solution was prepared by dissolving 1 wt.% chitosan, 1 wt.% acetic acid, and 0.2 wt.% glycerol in DI water at 80 °C. The rGO:AuNPs:chitosan solution was then prepared by mixing the rGO:Au solution with 1 wt.% chitosan solution (1:1 v/v ratio), followed by 1 h sonication.

2.2.2. Fabrication of LIG Reference Electrode (RE) and Working Electrode (WE)

PI tapes were first mounted onto a glass slide for laser scribing. Next, a LIG three-electrode system was created by a 30 W carbon dioxide (CO_2) laser (VLS2.30, Universal Laser Systems, Inc. VLS2.3) in a raster mode, utilizing 10.5% of the maximum power, 11% of the maximum speed, 1000 pixels per inch (PPI), and an image density of 6. A fabricated LIG RE was coated with 10 µL of commercially available Ag ink. The modified electrode with drop-cast Ag ink was dried on an 80 °C hot plate for 10 min. Subsequently, a solution containing 0.1 mmol of $FeCl_3$ was applied to the surface of the electrode for 1 min. The electrode was then rinsed with DI water and dried on the 80 °C hot plate for another 10 min. Next, the PVB reference mixture was created by dissolving 50 mg of NaCl, 79.1 mg of PVB, 1 mg of F-127, and 0.2 mg of MWCNT in 1 mL of methanol. The cocktail solution (20 µL) was applied onto the RE surface and allowed to dry at room temperature, followed by dropping and drying 10 µL of a 1 wt.% Nafion solution at the ambient condition to fabricate the silver/silver chloride (Ag/AgCl) LIG RE.

The modification of the LIG WE started with applying 20 µL of the synthesized 6:1 v/v rGO-AuNPs nanocomposite, followed by drying on a hot plate (80 °C) for 10 min. Electrodeposition of the Prussian blue (PB) on the nanocomposite-modified WE was performed by cyclic voltammetry (CV) (180 cycles) between 0 and 1 V (vs Ag/AgCl) at a scan rate of 0.1 V s^{-1} in a freshly prepared mixed solution of 2.5 mM $FeCl_3$, 2.5 mM $K_3Fe(CN)_6$, 0.1 M KCl, 0.1 M HCl, and 0.2 mM $HAuCl_4$.

Next, a LOx solution was prepared by mixing a chitosan solution (2 wt.% chitosan, 2 wt.% acetic acid, and 0.8 wt.% glycerol dissolved in DI water at 80 °C). The chitosan solution was then mixed with the LOx enzyme solution (LOx dissolved in the DI water, 40 mg mL^{-1}) at a 1:1 (v/v) ratio. Simultaneously, a BSA solution (10 mg mL^{-1}) was prepared by dissolving BSA in the DI water. A LOx:BSA solution was then created by mixing the LOx solution and BSA solution at a 1:1 (v/v) ratio.

Following the PB electrodeposition and drying, 20 µL of LOx:BSA solution (PB-LOx-BSA) was placed on the WE. Subsequently, a Glu solution (25 wt.% stock solution diluted with DI water, 8 wt.%) was prepared as a blocking agent. The modified LIG WE with PB-LOx-BSA was then covered with 5 µL of an 8 wt.% Glu solution and then dried at ambient conditions. Finally, the enzyme-immobilized LIG sensor was incubated at 4 °C overnight before use (Figure S1A, Supporting Information).

2.3. Preparation of the pH Sensor Based on the LIG/Polyaniline Composites

A polyaniline (PANI) electrodeposition solution was prepared by mixing 0.1 M aniline and 1 M H_2SO_4 in distilled water and stirring until fully dissolved. The PANI electrodeposition on the LIG WE was performed using CV with a platinum rod as the counter electrode (CE), a voltage range from −0.2 to 1 V, and a scan rate of 0.1 V s^{-1} (Figure 4; Figure S1B, Supporting Information).[59] The pH sensor was calibrated by immersing it in buffer solutions with pH values ranging from 5 to 8. Prior to connecting the electrodes, the sensor was thoroughly rinsed with the buffer solutions to ensure adequate wetting of the modified surface for enhanced contact and reliability.

2.4. Fabrication of GHS-Integrated Microfluidic Patch

2.4.1. Fabrication of Wearable Microfluidic Device

The hydrophilicity of PDMS is modified by adding commercially available surfactant PEG-PDMS BCP (2.5 wt.%) to the PDMS (silicone elastomer base: curing agent = 10:1 (w/w)) before curing. This mixture was vacuumed at 700 mmHg until no bubbles were observed. Subsequently, it was cured in an 80 °C oven for 20 min. The PEG-PDMS[60] was patterned to create coil-shaped microfluidic channels and inlet/outlet wells through laser engraving by

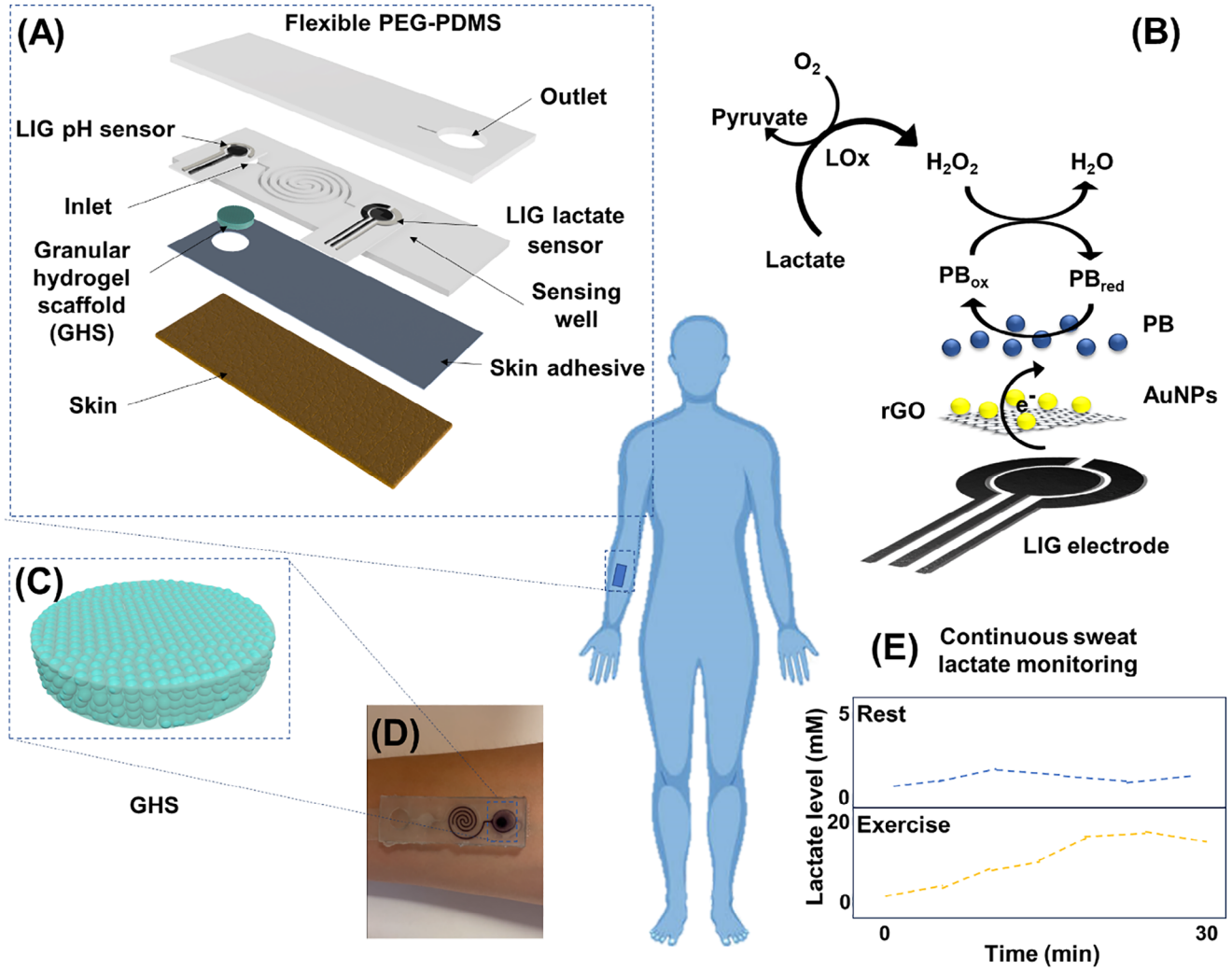

Figure 1. Schematic showing the design, structure, and application of the wearable microfluidic enzymatic sweat sensing patch: A) Exploded view of the patch that integrates electrochemical lactate and pH sensors with a microfluidic platform based on hydrophilic PEG-PDMS, as well as the GHS for sweat collection. B) Working principle of modified LIG nanocomposite lactate sensor. C) GHS is integrated into the inlet of the microfluidic patch for rapid sweat collection. D) Optical image showing an individual's wearable patch on the forearm. E) On-body lactate measurements with the wearable lactate sensing patch at rest or exercise (qualitative representation).

a 30 W CO_2 laser using the raster mode (11% of the maximum speed, 10.5% of the maximum power, 1000 PPI, and image density = 6). The channels were flushed with deionized water following laser engraving to eliminate any remaining PEG-PDMS residuals (**Figure** 1A; Figure S1C, Supporting Information). See the design and fabrication procedure in Figures S1 and S2 (Supporting Information).

2.4.2. Fabrication of Step-Emulsification Microfluidic Devices for Droplet Production

Step-emulsification microfluidic devices for high-throughput droplet production were fabricated at the nanofabrication facilities (Penn State) according to soft lithography procedures.[48,61] Briefly, master molds were created on silicon wafers (University Wafers, MA, USA) using KMPR 1000 series negative photoresists (Kayaku Advanced Materials, MA, USA). Next, microfluidic devices were molded using PDMS (a 10:1 mass ratio of the base and crosslinker mixture), then poured onto the masters, and cured at 80 °C for 2 h. PDMS devices were bonded to glass slides after air plasma treatment.

2.4.3. Synthesis of Gelatin Methacryloyl (GelMA) Polymer

GelMA synthesis was conducted following an established method.[62] Gelatin was dissolved in 200 mL of a DPBS solution at 50 °C. Subsequently, 16 mL of methacrylic anhydride was added dropwise to the gelatin solution, which was shielded with aluminum foil to prevent light exposure. The reaction was stopped after 2 h by adding 400 mL of excess DPBS. The resulting solution was then dialyzed against ultrapure (Milli-Q) water at 40 °C using 12–14 kDa molecular weight cutoff (MWCO) membranes

(Spectrum Laboratories, NJ, USA) for 10 days. The solution was filtered using a vacuum filtration unit with a pore size of 0.20 µm (VWR, PA, USA) and frozen at −80 °C, followed by lyophilization (Labconco FreeZone 4.5L Benchtop Freeze Dryer, MO, USA) to yield solid GelMA, which was stored in the fridge for further use.

2.4.4. Microgel Fabrication

GelMA microgels were prepared using the step emulsification microfluidic devices following an established protocol.[63] First, droplets were formed in a surfactant-stabilized water-in-oil emulsion. The aqueous phase consisted of GelMA polymer (concentration = 10% w/v dissolved in DPBS), containing 0.1% w/v of photoinitiator LAP. The continuous oil phase comprised the Novec 7500 Engineered Fluid and Pico-Surf surfactant (2% v/v). Syringe pumps (PHD 2000, Harvard Apparatus, MA, USA) were used to inject oil and aqueous phases into the step emulsification device. The setup was covered with aluminum foil to prevent light exposure, and the temperature was maintained at 35–40 °C. After emulsion formation, the droplets were collected and physically crosslinked via overnight incubation at 4 °C, yielding GelMA microgels.

2.4.5. Formation of GHS

The oil and surfactant were washed from the stable microgels using PFO (20% v/v in the Novec 7500 Engineering Fluid). Next, a LAP solution (0.1% w/v in DPBS) was added to yield a microgel suspension, followed by packing via centrifugation at 3000 ×g for 15 s. The microgel suspension was then transferred to a cylindrical mold (diameter = 8 mm, height = 1 mm) using a positive displacement pipette (Microman E M100E, Gilson, WI, USA) and photocrosslinked via light exposure (wavelength ≈400–405 nm, intensity = 15 mW cm^{-2}, exposure time = 1 min) to form GHS. Accordingly, GHS comprised photocrosslinked GelMA microgels that were covalently interlinked.

2.4.6. GHS Pore Visualization

To visualize GHS void spaces, a high molecular weight FITC-dextran (M_w ≈2 MDa, 15 µM in ultrapure water) was pipetted on the scaffold surface. This biomolecule was unable to penetrate the microgels but filled the void spaces among them within the GHS. Fluorescence microscopy (Leica DMi8 with THUNDER imaging system, Leica Microsystems, Germany) was conducted to acquire *Z*-stack images of GHS, showing the void spaces in green. Leica software (LAS X, version 5.1.0) was used for 3D renderings, enabling the visualization of interconnected void spaces within the GHS.

2.4.7. Integration of the Wearable Microfluidic Channels with GHS

Plasma treatment was performed for 45 s under 400 mTorr pressure using a PDC-001-HP (Harrick Plasma) device to increase the hydrophilicity of PEG/PDMS microfluidic devices. The PEG/PDMS top and bottom layers were placed in the equipment chamber with the channel side facing up. The vacuum pump was then activated to reduce the atmospheric pressure to below 400 mTorr. After setting the Plasma power to high, the 5-min countdown began once the purple plasma glow appeared inside the chamber. After the 5-min treatment, the fabricated LIG sensor was positioned within a sensing chamber on the bottom microfluidic layer of PEG-PDMS, followed by the assembly of two PEG-PDMS layers after plasma treatment. Subsequently, the GHS was integrated into the inlet for enhanced sweat collection. A skin adhesive layer was used between the assembled device and human skin for on-body measurements (Figure S1D, Supporting Information).

2.5. Characterizations

2.5.1. Characterization of Materials

The rGO-AuNPs modified LIG electrode was characterized by field emission scanning electron microscopy (FESEM) to study metal particle dispersion in the composite. Energy dispersive spectroscopy (EDS) was used to analyze the elemental composition of the synthesized composite (EDS feature integrated with SEM on Machine FESEM Apreo 5, voltage: 3 kV, beam current = 13 pA). Transmission electron microscopy (TEM) with a Talos TEM (Thermo Scientific) was conducted to analyze the crystalline structure of rGO-AuNP nanocomposite. The X-ray diffraction (XRD) pattern of the rGO-AuNP nanocomposite was obtained using a D8 Discover X-ray diffractometer (Bruker Corporation, Massachusetts, USA).

2.5.2. Characterization of Wearable Microfluidic Device

The sweat uptake capability of the microfluidic channels integrated with (experimental group) or without (control group) the GHS in the inlet chamber was evaluated in vitro by pumping an aqueous solution, containing 5 mL of deionized water containing 100 µL of red food dye at a flow rate of 500 nL min^{-1} using a syringe pump (New Era Pump Systems, Inc). The assembled microfluidic device was clipped between two 1.5 mm thick PMMA boards with laser-cut (30 W CO_2 laser, VLS2.30, Universal Laser Systems, Inc. VLS2.3) inlet, outlet, and holes for screws. A Nikon D7500 camera (Nikon Inc., USA) was used to capture the microfluidic flow and determine the time for the flow to travel from the inlet to the outlet. (Figure S3A,B, Supporting Information). Photographs were captured at 10-min intervals to track the solution flow within the channels until reaching the outlet. Concurrently, the flow rate for each time-lapse image was derived by computing the ratio of the aqueous dye solution's volume to the elapsed time.

2.5.3. On-Body Evaluation of the Integrated Wearable Microfluidic Device

The human subject went through an initial warm-up of 5 min, followed by low-, medium-, and high-intensity cycling for 15 min.

The sweat was collected every 5 min, with sweat and blood lactate measured in the subsequent 2 min.[64] The detailed human subject testing was approved by the Institutional Review Board (IRB) at Penn State University (IRB #STUDY00020880).

2.6. Statistical Analyses

The statistical analyses were conducted with a minimum of three samples per group ($n \geq 3$). One-way analysis of variance (ANOVA) followed by Tukey's multiple comparison test with a 95% confidence interval was performed using GraphPad Prism (version 10.4.1, CA, USA).

3. Results and Discussion

3.1. Device Structure

The wearable microfluidic sensing device consists of electrochemical lactate and pH sensors, together with a flexible microfluidic platform featuring coiled channels and a GHS within the inlet reservoir (Figure 1A). The nanocomposite-modified porous LIG electrochemical lactate sensor with a three-electrode configuration is enclosed within the coil-shaped microfluidic channel (Figure 1B; Figure S1, Supporting Information). The flexible and stretchable microfluidic device based on the PEG-PDMS with increased hydrophilicity is integrated with the GHS, made up of photo-assembled GelMA microgels, in the inlet (Figure 1C). The soft and wearable sweat sensing patch can be comfortably attached to various locations of the human body, such as the arm (Figure 1D), enabling sweat collection and analysis (Figure 1E).

3.2. Design and Characterization of the Wearable Microfluidic Device

Compared with the sweat secretion rate during physical activities, the rate at rest or during sedentary activities is significantly reduced.[10] The compact coil-shaped microfluidic channel (Figure S2, Supporting Information) with increased surface area is designed to improve fluid transport and minimize sweat loss, contributing to accuracy and sensitivity.[65–67] The capillary action inherent to hydrogels, 3D networks of crosslinked hydrophilic polymers with high water absorption and retention capacity,[68] can be significantly enhanced in the porous GHS architecture, constructed from GelMA-based spherical microgels. The GHS increases absorbance by synergizing the advantages of hydrogels and the large specific surface area of granular materials.[69] The capillary effect in GHS relies on various factors, including the size, shape, and surface properties of microgels, as well as the characteristics of the absorbate. To integrate the GHS in the wearable microfluidic device (**Figure 2A**), GHS is first fabricated by photocrosslinking jammed GelMA microgel building blocks of varying sizes: small (GHS-S, microgel diameter $D = 28 \pm 3$ µm), medium (GHS-M, $D = 80 \pm 4$ µm), and large (GHS-L, $D = 184 \pm 9$ µm). The large fluorescent biomolecules that fill the interstitial void spaces, followed by 3D imaging, help visualize the porous structure of GelMA GHS (Figure 2B). After placing GHS-S, GHS-M, GHS-L, or a bulk hydrogel counterpart (control) in the wearable microfluidic device, bringing an aqueous solution in contact with the hydrogels highlights the effect of pore size on the fluid uptake (Figure 2C). GHS enables fluid transport through microscale void spaces among the microgels. The channel filling time follows GHS-S > GHS-M > GHS-L, though statistically non-significant (Figure 2D). The bulk hydrogel counterpart, lacking interconnected void spaces, fails to absorb the dye in 120 s. All the GHS have a similar void fraction, reported as 20%–25%.[48] GHS-S and GHS-M, with a median equivalent pore diameter of 12 ± 1 and 20 ± 1 µm, absorb the dye and fill the sensing chamber after 76 ± 15 and 70 ± 15 s, respectively. With a median equivalent pore diameter of 41 ± 2 µm, the GHS-L fills the sensing chamber in 53 ± 7 s, which is not significantly lower than the other GHS.

To mimic natural sweat secretion at rest and study the sweat sampling against gravity, the fabricated microfluidic device with GHS-L integrated into the inlet chamber was placed into a PMMA chip system, with the sweat-mimicking solution containing a red dye pumped at a flow rate of 500 nL min^{-1} (Figure S3A,B, Supporting Information). The provided sweat-mimicking solution near the microfluidic device inlet is absorbed and transferred by the GHS to the microfluidic channel, filling the detection well. The sweat-mimicking solution accumulated in the control (no-hydrogel inlet) falls short of gathering a sufficient liquid volume to fill the inlet and facilitate fluid transfer to the microfluidic channel within the designated 60-min timeframe (Figure S3C, Supporting Information).

3.3. Design and Characterization of the LIG Nanocomposite-Based Electrochemical Lactate Sensor

The specific identification of target biomarkers in the complex sweat mixture of analytes, including ions and proteins, requires sensitive and selective three-electrode flexible biosensors (Figure S4A, Supporting Information). After the electrodeposition of PB, the LOx enzyme is immobilized on the WE surface (Figure S4B, Supporting Information). As a mediator to enhance the transfer of electrons between the electrode surface and immobilized enzyme, PB on the WE facilitates the conversion of lactate to a measurable electrical signal. The sensitivity is maximized by optimizing the CV electrodeposition process of PB on the LIG-based WE, achieved by varying the cycle from 30 to 180, with the peak achieved at the cycle of 180 (Figure S4C, Supporting Information). Furthermore, immobilizing and blocking agents can enhance the stability and selectivity (due to minimized nonspecific binding) of the sensor, respectively. Because of the dual role of BSA in immobilizing/blocking[70] and Glu in crosslinking,[71,72] they are explored for enzyme immobilization on the LIG surface and performance optimization. The comparison in the oxidizing activity of LIG-LOx modified with drop-cast BSA (LOx-BSA), BSA and Glu (LOx-BSA-Glu), and chitosan and Glu (LOx-chitosan-Glu) shows the effects of different immobilizing, blocking, and crosslinking agents on the sensing activity of LOx. The CV curves for LOx, LOx-BSA, LOx-BSA-Glu, and LOx-chitosan-Glu (Figure S4D, Supporting Information) indicate that the LOx-BSA-Glu composite has the highest sensitivity, attributed to its optimized enzyme stability. The combination of optimized PB

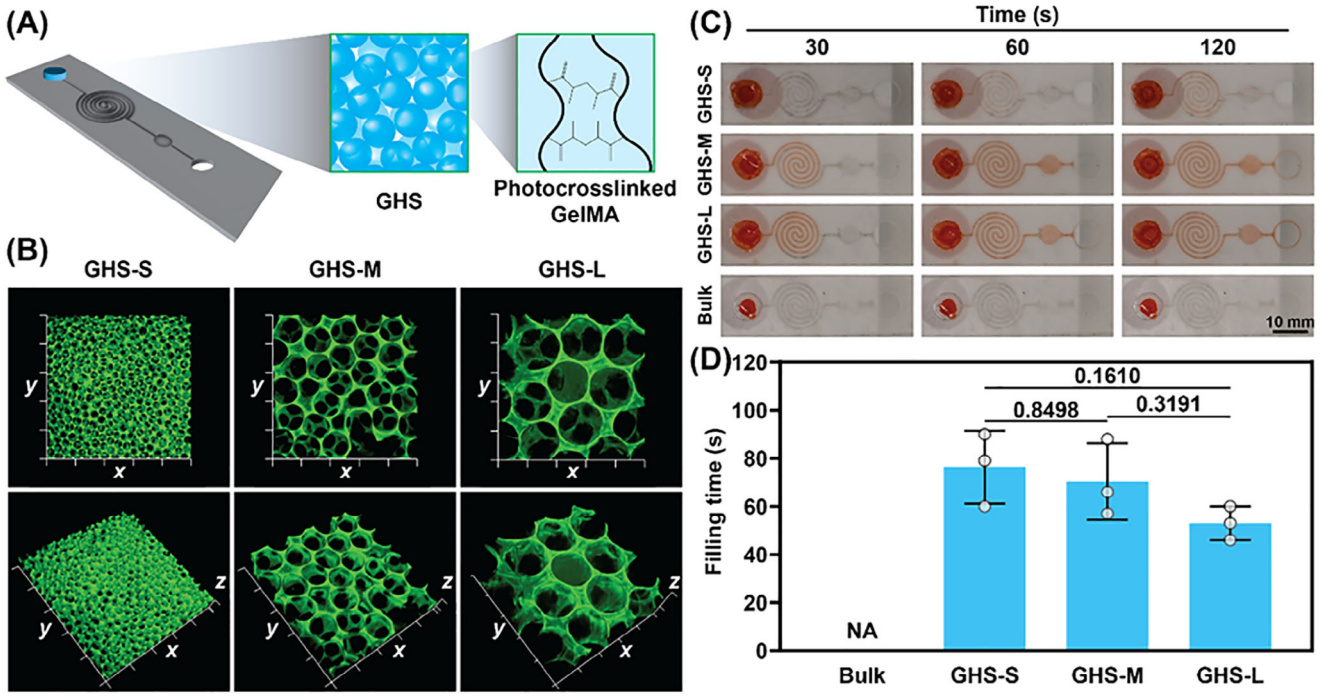

Figure 2. GHS characterization and integration into the microfluidic sensing device. A) Schematic illustration of the microfluidic device, equipped with the GHS, composed of photo-assembled GelMA microgels. B) Top and 3D orthogonal views of *Z*-stacked fluorescence images, showing the void spaces (green) among small, medium, or large microgels in GHS-S, GHS-M, or GHS-L, respectively. Increments are 100 µm. C) Images of the microfluidic device, showing solution transport via the GHS or bulk hydrogels in the microfluidic channels over time. D) Sensing chamber filling time using the GHS-L, GHS-M, and GHS-S, as well as the bulk hydrogel counterpart serving as a negative control representative of conventional non-porous hydrogels (did not fill the chamber). The *p*-values are calculated using the one-way ANOVA, followed by Tukey's multiple comparisons test with a 95% confidence interval.

and LOx-BSA-Glu shows an even higher sensitivity with a 7.78-fold increase when compared with the bare LIG electrode (Figure S4E, Supporting Information). In the amperometry test with consecutively added L-lactic acid in 0.1 M PBS (pH 7) (Figure S4F, Supporting Information), the PB-modified LIG with LOx-BSA-Glu (PB-LOx-BSA-Glu) electrode demonstrates a sensitivity of -10.93 µA mM^{-1} cm^{-2} in the concentration range from 0.1 to 0.4 m (Figure S4G, Supporting Information) and -1.58 µA mM^{-1} cm^{-2} from 0.5 to 40 mM (Figure S4H, Supporting Information). The synergistic integration of optimized immobilizing, blocking, and crosslinking agents in the PB-LOx-BSA-Glu nanocomposite-modified LIG electrode significantly enhances sensitivity and selectivity across a broad sensing range in complex sweat mixtures.

Further sensitivity enhancement may originate from the integration of conductive nanomaterials into the porous LIG framework to increase the surface area, streamline electron transfer, and boost the electrocatalytic electrode performance (Figure S5, Supporting Information). The schematic in **Figure 3**A shows the processes to decorate the rGO-AuNPs nanocomposites and immobilize enzymes on the surface of LIG WE. The morphology and dispersion of the AuNPs with different volume ratios to rGO in the nanocomposite show the formation of Au nanoscale dendrites at the optimized ratio of 6:1 (Figure S5A–C, Supporting Information). Relatively uniform distribution is achieved in the rGO-AuNPs nanocomposite with the optimized ratio, as evidenced by individual elements based on their weight and atom percentages in the FESEM and EDS characterizations (Figures S6 and S7, Supporting Information). In contrast, the higher AuNPs ratios (i.e., 1:1 and 3:1) in the composite result in poorly dispersed round-shaped metals in the carbon matrix with agglomeration on the edges of GO sheets and wrinkles (Figure S8, Supporting Information). Further characterization of the nanocomposite with the TEM analysis and elemental mapping indicates a uniform dispersion of well-defined gold nanoparticles on the reduced graphene oxide (rGO) surface (Figure S9, Supporting Information). The comparison in the CV curves of electrodes with three different rGO:AuNPs volume ratios also confirms the highest sensitivity from the ratio of 6:1 v/v (Figure S5E, Supporting Information), attributed to the significantly higher surface area in the dendrite morphology with a highly branched, tree-like structure (compared with spherical AuNPs).[73] The unique dendrite morphology of Au also provides a larger number of exposed crystals, as revealed by peaks corresponding to the (111), (200), (220), and (311) planes in the XRD characterization (Figure S10, Supporting Information). The strong peak at 38.1° indicates that the nanoparticles predominantly grow in the {111} direction, such as {111} and {110}, with enhanced electron transfer and electrochemical activity (Figure S10, and S5E, Supporting Information). The FESEM, EDS, TEM, and XRD characterizations consistently highlight the contribution of crystalline structure, near-uniform distribution, and successful integration of gold nanoparticles on the rGO surface to enhance sensing.

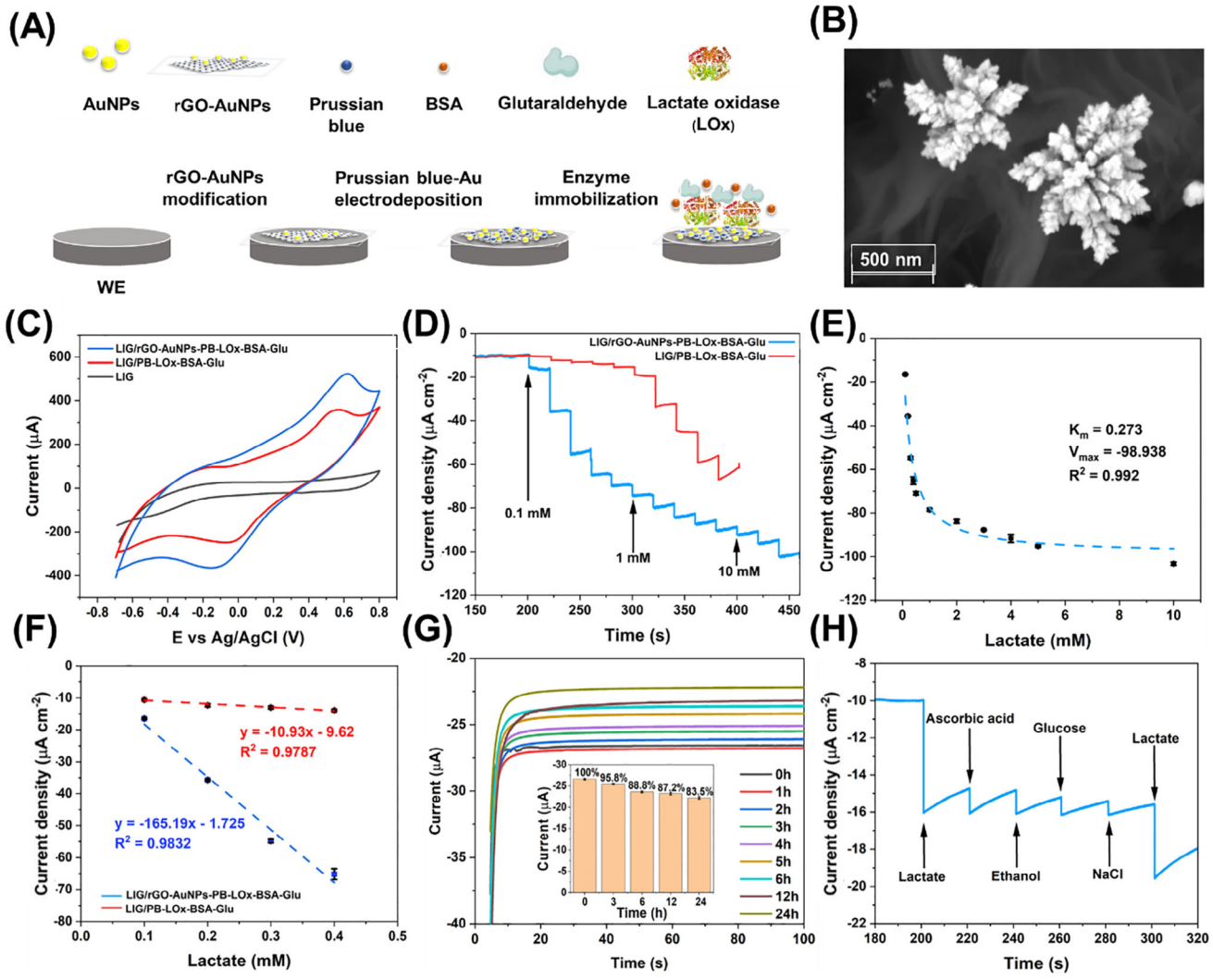

Figure 3. In vitro characterization of the LIG-based lactate sensor. A) Schematic of LIG WE decoration with nanocomposites and enzyme immobilization. B) The FESEM image of rGO-AuNPs nanocomposite. C) The CV curves of WE based on bare LIG, LIG/PB-LOx-BSA-Glu, and LIG/rGO-AuNPs-PB-LOx-BSA-Glu in response to 1.0 mM L-lactic acid in 0.1 M PBS (pH 7) with a scan rate of 50 mV s^{-1}. D) Amperometric response of the WE based on LIG/PB-LOx-BSA-Glu and LIG/rGO-AuNPs-PB-LOx-BSA-Glu to consecutively injected L-lactic acid in stirred 0.1 M PBS (pH 7) with an applied potential of −0.05 V at 37 °C, and E) the Michaelis–Menten fit for the LIG/rGO-AuNPs-PB-LOx-BSA-Glu WE. F) Comparison of in vitro calibration curves between the sensors with LIG/PB-LOx-BSA-Glu and LIG/rGO-AuNPs-PB-LOx-BSA-Glu WE. G) Response stability of the optimized LIG/rGO-AuNPs-PB-LOx-BSA-Glu sensor to 1 mM lactate at 1 h intervals over 24 h, with the corresponding sensitivity graphs shown in the inset (the sensor was maintained at the ambient condition during consecutive runs). H) Selectivity study with the optimized LIG/rGO-AuNPs-PB-LOx-BSA-Glu sensor, responding to 1 mM lactate, 25 μM ascorbic acid, 50 μM ethanol, 0.1 mM glucose, and 0.1 mM NaCl (at −0.05 V).

The AuNPs and PB (PB-AuNPs) could be in situ co-electrodeposited using CV or chronoamperometry (CA) (Figure S11, Supporting Information). The resulting electrode with LOx immobilized by the in situ co-electrodeposited PB-AuNPs (LIG/rGO-AuNPs-PB-LOx-BSA-Glu) has superior electrocatalytic activity toward lactate electrooxidation compared with bare LIG and LIG modified with PB-LOx-BSA-Glu (Figure 3C). Therefore, this optimized sensor design is used in the subsequent investigations unless otherwise specified. The amperometric detection of consecutively injected L-lactic acid into the stirred 0.1 M PBS (pH 7) at −0.05 V with the optimized sensor shows a low limit of detection (LOD) of 0.0258 μM and high sensitivity of −165.19 μA mM^{-1} cm^{-2} for the lactate concentration ranging from 0.1 to 0.4 mM (Figure 3D–F). The sensitivity is ≈15-fold higher than that of the LIG/PB-LOx-BSA-Glu sensor (−10.93 μA mM^{-1} cm^{-2}) with a LOD of 0.39 μM at 0.1–0.5 mM of lactate (Figure S4G).

The current response changes rapidly with the progressive addition of L-lactic acid, achieving 95% of the steady-state current within 3–5 s, based on a single concentration in the absence of interfering species. The relationship between the rate of an enzyme-catalyzed reaction and the concentration of target molecules can be described by the Michaelis–Menten equation[74] (see Section S1.4, Supporting Information for details). The fitting of the equation determines the kinetic parameters pertaining to the behavior of LOx (Figure 3E; Figure S12, Supporting Information). The sensor stability can be revealed by the key parameters

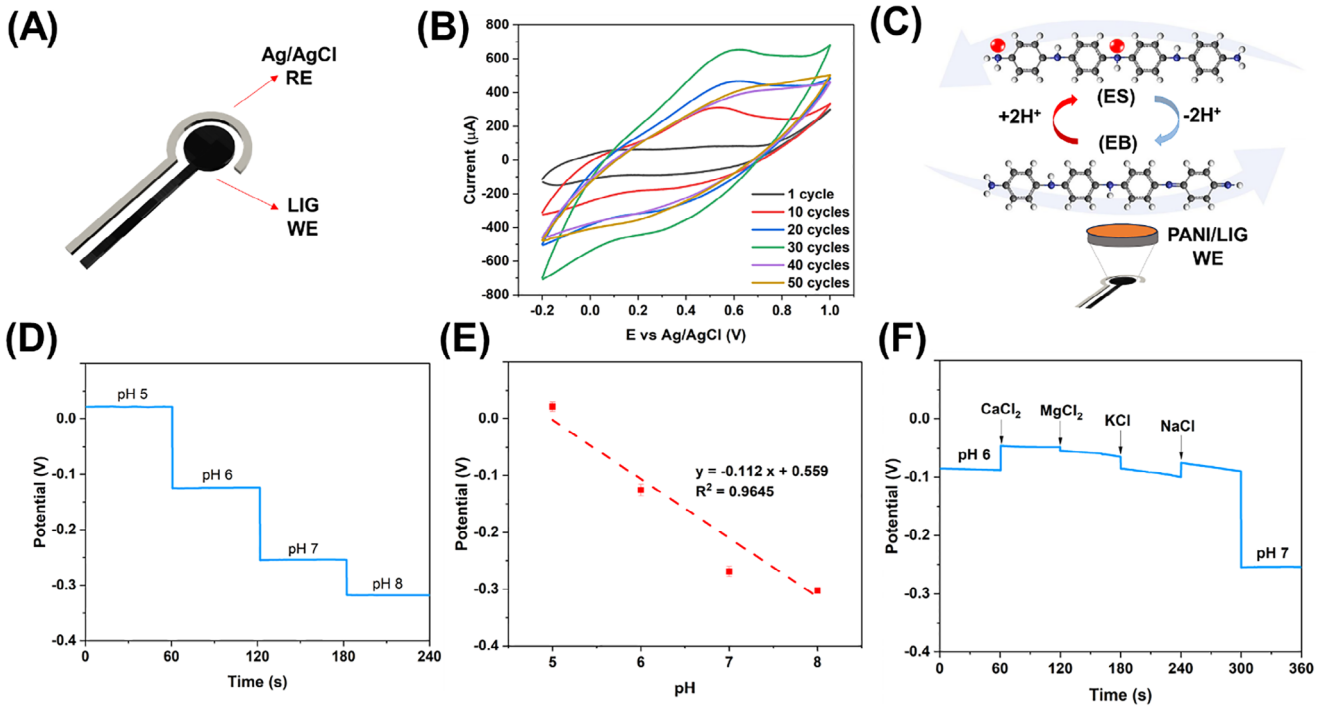

Figure 4. In vitro characterization of the LIG/PANI pH sensor: A) Schematic of the two-electrode design. B) CV curves of LIG WE, modified with different electrodeposited cycles of PANI. C) The mechanism of electrochemical pH detection on the LIG WE modified with PANI. D) The OCP of the PANI/LIG sensor in different pH buffer solutions and E) the corresponding calibration curve. F) The selectivity of the pH sensor to 1 mM $CaCl_2$, 1 m $MgCl_2$, 8 mM KCl, and 20 mM NaCl.

of Michaelis-Menten kinetics (i.e., V_{max} and K_m). The comparison in V_{max} and K_m before and after 8 h usage indicates minimal changes in the sensor performance (Figure S13, Supporting Information). In particular, V_{max} slightly changes from the initial value of ≈−199 to ≈−189 after 8 h (≈5%), which indicates negligible enzyme deactivation or degradation. Meanwhile, the constant K_m suggests a stable binding affinity between the enzyme and substrate or unchanged active sites of the enzyme. In addition, the flexible enzymatic LIG-based lactate sensor undergoes only ≈4% current loss upon mechanical bending (Figures S14 and S15, Supporting Information).

In addition, the 24-h stability of the LIG-based lactate sensor is assessed. The current response of the sensor also retains 83.5% of sensitivity after 24 h (after storage under ambient conditions) (Figure 3G) and over 95% after 30 runs (at a fixed lactate concentration) (Figure S16, Supporting Information), indicating excellent reproducibility and minimal signal degradation. These results validate the robustness of the LOx-BSA-Glu immobilization strategy and highlight the device's suitability for continuous or repeated lactate monitoring in wearable applications. The selectivity of lactate is also examined over commonly used interfering species, including ascorbic acid, ethanol, glucose, and NaCl (Figure 3H). The current density measured from 12 individual sensors in a controlled PBS environment with varying concentrations of lactate (0.1, 0.5, and 1 mM) at 0.05 V have consistent median values (−15.6, −71.1, and −78.5 μA cm^{-2}) and relatively low standard deviations (ranging from 0.64 to 1.73 μA cm^{-2}), indicating sensor-to-sensor reproducibility (Figure S16A–C, Supporting Information). Device-level reproducibility was confirmed by the relatively low variability in current densities (−43 ± 3, −163 ± 5, and −183 ± 6 μA cm^{-2} measured across three independently tested devices in artificial sweat containing 0.1, 0.5, and 1 mM lactate, respectively (Figure S17D, Supporting Information).

3.4. Design and Characterization of the pH Sensor

To measure varying sweat pH levels (pH = 5–7) for accurate lactate detection, PANI electrodeposited onto the LIG WE using CV yields a two-electrode LIG pH sensor (**Figure 4A**). The increase in the scan number ranging from 10 to 50 identifies the optimal value of 30 cycles for the highest peak current, with a significant oxidation peak at ≈0.66 V during the forward scan at 1.0 V and a minor reduction peak around 0.1 V during the reverse scan (Figure 4B). Polyaniline is an excellent candidate for flexible pH sensors due to its high conductivity, environmental stability, and ability to undergo reversible doping, allowing rapid and durable response to pH changes.[75] In acidic environments (lower pH), PANI in its conductive emeraldine salt (ES) form has fully protonated polymer chains and exhibits high conductivity. As the pH increases, deprotonation occurs to gradually reduce the conductivity of polyaniline as it transitions to its non-conductive emeraldine base (EB) form at higher pH levels (Figure 4C).[76]

As a result, the conductivity changes measured by the open-circuit potential (OCP) directly depend on the pH, with a notable sensitivity of ≈ −111.99 mV pH^{-1} (Figure 4D,E). The pH sensor also has a reasonably high selectivity over different common ions in sweat (e.g., Ca^{2+}, Mg^{2+}, K^+, and Na^+)[77] at pH = 6

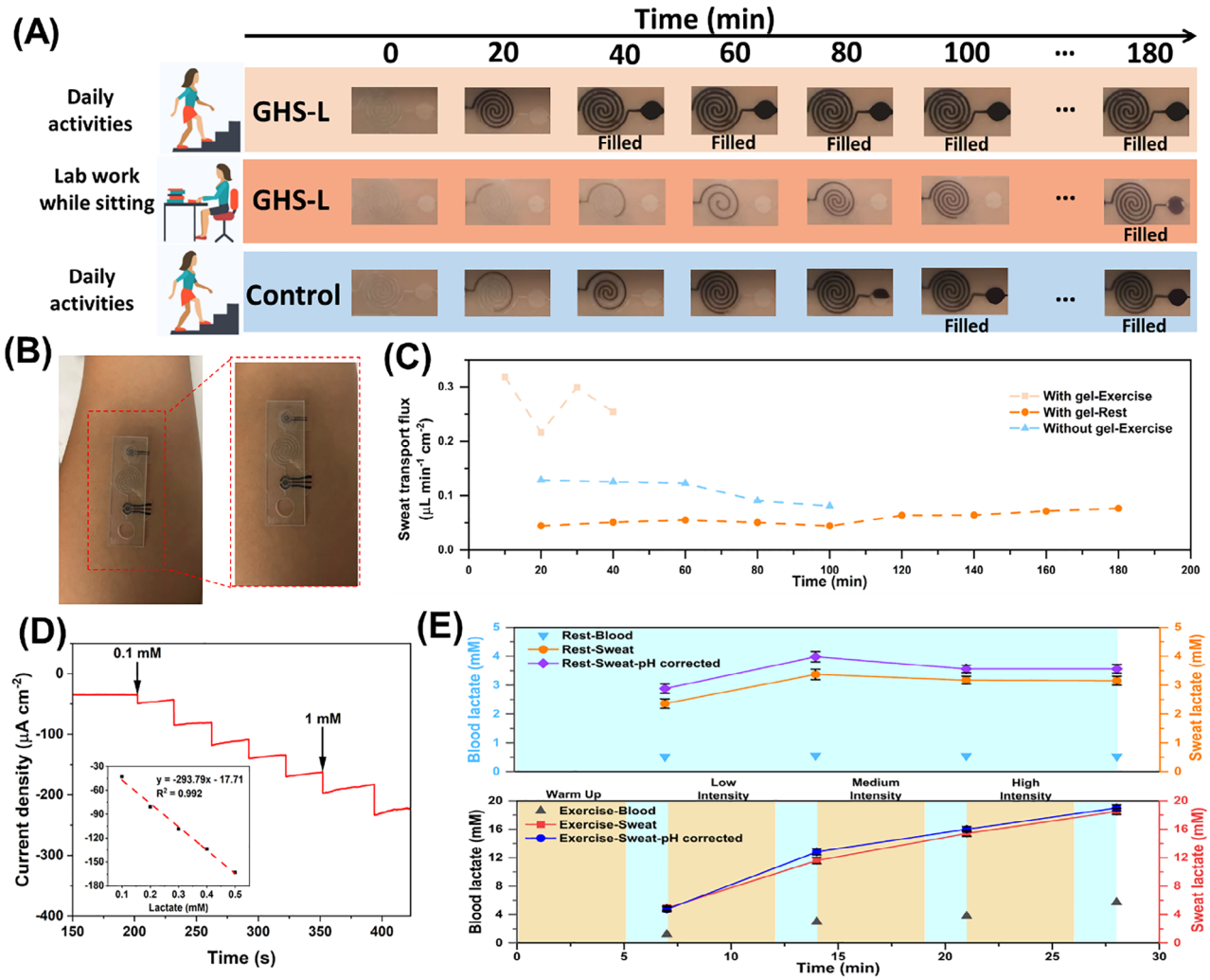

Figure 5. Characterization of the LIG nanocomposite-based lactate sensor, integrated with a GHS-equipped microfluidic patch for on-body sweat analysis. A) Optical images of sweat collected in the GHS-L-equipped microfluidic patch and a hydrogel-free control on a human subject during two different physical activities over time. B) Optical images showing a wearable sensing patch on the forearm of an individual with an enlarged view of the patch on the right, and C) measured sweat transport flux. D) The amperometric response of the integrated microfluidic sensing system to consecutively injected L-lactic acid of varying concentrations into the artificial sweat (applied potential = −0.05 V), with the corresponding calibration curve shown in the inset. E) Comparison of sweat lactate levels, measured by the microfluidic patch with gold standard blood lactate levels during rest and daily activities at three different intensities. Sweat lactate, collected over 5 min and measured over the following 2 min, with blood lactate levels recorded simultaneously during the 2-min measurement period. The calibration of the lactate measurement with simultaneously measured pH. All data are represented as mean ± SD from three independent measurements.

(Figure 4F), confirming its robustness in physiologically relevant conditions. Together with minimal signal degradation (≈10%) over 10 repeated measurement cycles (Figure S18, Supporting Information), our pH sensor compares favorably with previously reported flexible and wearable pH sensing platforms (Table S1, Supporting Information).

3.5. Calibration of the Lactate Measurement with Simultaneous pH Measurement

The in vitro evaluation of the lactate sensor in the lactate solution (10–50 μM) with varying pH levels from 5 to 7 indicates a strong pH effect on the amperometric current signal through the slope and intercept of the linear calibration curve (Figure S19, Supporting Information). Meanwhile, the simultaneously measured pH also allows the calibration of measured lactate values against pH for improved accuracy (Tables and S4, Section S1.5 Supporting Information).

3.6. On-Body Evaluation of the Wearable Lactate Sensor Patch

Using a skin adhesive medical tape, the sensor with a GHS-L-incorporated microfluidic patch is attached to the arm for continuous sweat collection and analysis (**Figure 5B**). While the integrated device accumulates sufficient sweat for lactate analysis after 40 min walking with a flow rate of ≈539 nL min^{-1} cm^{-2}, it

takes ≈180 min with 119 nL min^{-1} cm^{-2} when the human subject performs lab work while sitting (Figure 5A–C). The GHS-L-incorporated microfluidic patch demonstrates a twofold increase in sweat collection time compared with the control (without any hydrogel modification), allowing for near-real-time sweat analysis (Figure 5A–C). Compared with the sweat transport flux of 2.8–57 nL min^{-1} cm^{-2} previously reported in the literature,[38] the sweat transport flux, ranging from 119 to 539 nL min^{-1} cm^{-2}, from this work is ≈9.5–42.5 times higher at the lower or higher sweat rate, providing faster and more efficient sweat accumulation and biomarker analysis, especially under low sweat secretion conditions (Table S4, Supporting Information).

Optimal control of fluid flow in microfluidic devices may boost analyte transport, enabling higher sensitivity and faster responses.[78,79] Therefore, the optimized enzymatic sensor based on the LIG/rGO-AuNPs-PB-LOx-BSA-Glu nanocomposite is integrated with the microfluidic device for in vitro performance evaluation and demonstration (Figure S20, Supporting Information). The calibration curve of the sensor's amperometric response to consecutively injected L-lactic acid in PBS leads to a sensitivity of ≈−310.66 µA mM^{-1} cm^{-2} and a low LOD of ≈0.011 µM (Figure S20, Supporting Information). These performance metrics surpass those of recently published enzymatic LIG-based lactate sensors, exhibiting sensitivities at least six times higher than previously reported counterparts (Table S5, Supporting Information).[80] Compared with PBS, artificial sweat has a more complex composition, including additional electrolytes (e.g., potassium, calcium, and magnesium ions) and organic compounds such as urea to mimic the chemical composition of human sweat. Different from the pH of 7 for PBS, a slightly acidic pH ranging from 4 to 6 is observed in artificial sweat to match the pH range of real human sweat.[81] Therefore, the sensor is calibrated in the artificial sweat in vitro using varying lactate concentrations before the on-body measurements (Figure 5D). The calibration curve of the amperometric response of the integrated device to different concentrations of L-lactic acid in the artificial sweat shows a sensitivity of ≈−293.79 µA mM^{-1} cm^{-2} (Figure 5D). The difference in the sensing response between PBS and artificial solutions is attributed to the varied composition and characteristics of the electrolyte solution. Although the sensitivity slightly decreased in artificial sweat, it remains significantly higher than previously reported values[82–85] due to the integration of the nanocomposite and the enzyme stabilization modification on the WE. The sweat lactate measured from the human subject during rest, low-, medium-, and high-intensity cycling every 5 min, each followed by a 2-min measurement period, shows a consistent trend with blood lactate levels captured by a commercial monitor[86] (THE EDGE Lactate Meter) (Figure 5E). With the simultaneously measured sweat pH, the on-body sweat lactate levels are further calibrated against pH (Section S1.6, Supporting Information) for more accurate lactate measurements (Figure 5E). The lactate concentration in sweat increases by increasing the exercise level. The integrated device with the GHS-L-incorporated microfluidic patch and the optimized enzymatic sensor based on the LIG/rGO-AuNPs-PB-LOx-BSA-Glu nanocomposite demonstrates remarkable performance in near-real-time lactate analysis during normal daily activities. Despite the erratic and intermittent nature of sweat production, the integrated device system exhibits a significant improvement in efficiency compared with controls, highlighting the importance of fluid flow and sweat collection optimization. The sensing platform, with excellent performance parameters such as high sensitivity, low LOD, and rapid response, particularly in artificial sweat, underscores its potential for accurate and dynamic non-invasive healthcare monitoring during daily activities.

4. Conclusion

This work presents the development and implementation of a highly sensitive wearable microfluidic sweat sensing platform, integrated with porous GHS, for the rapid uptake and analysis of sweat at low secretion rates. The microfluidic device with GHS-L integrated into the inlet chamber can collect the sweat with a transport flux from ≈119 to ≈539 nL min^{-1} cm^{-2} during low-intensity (e.g., sitting) and moderate (e.g., walking) daily activities, which is more than ten times higher than the other literature reports. The electrochemical sensor based on the optimized LIG nanocomposite electrode in the integrated device also exhibits an excellent sensitivity of ≈−310.66 µA mM^{-1} cm^{-2} and a low LOD of ≈0.011 µM for lactate sensing. The proof-of-concept demonstration features a cost-effective, sensitive, and versatile flexible sensing platform for early biomarker detection, where sweat production is minimal or sporadic, e.g., at rest or during mild physical activities. The demonstrated sensing system can also be readily adapted to detect other biomarkers by using corresponding enzymatic sensors in the integrated device. The advancement of non-invasive sweat analysis during daily activities with a cost-effective, flexible microfluidic sweat-sensing patch may open opportunities for personalized medicine and population health.

Supporting Information

Supporting Information is available from the Wiley Online Library or from the author.

Acknowledgements

F.L. and X.Z. contributed equally to this work. H.C. acknowledged the support from the National Institutes of Health (Award Nos. R21EB030140, U01DA056242, and R21OH012220), the National Science Foundation (NSF) (Grant Nos. 2309323, 2319139, and 2243979), and Penn State University. A.D. would like to acknowledge the National Institutes of Health grant (T32NS115667) and the Leighton Riess Graduate Fellowship at Penn State. Z.A. acknowledged the Diefenderfer Graduate Fellowship in Entrepreneurship. A.S. acknowledged the Penn State startup fund, Dorothy Foehr Huck and J. Lloyd Huck Early Career Chair in Biomaterials and Regenerative Engineering, the support of the Convergence Center for Living Multifunctional Material Systems (LiMC^2), and the Cluster of Excellence Living, Adaptive and Energy-autonomous Materials Systems (livMatS) Living Multifunctional Materials Collaborative Research Seed Grant Program, and the Materials Research Institute (MRI) and the College of Engineering Materials Matter at the Human Level seed grants.

Conflict of Interest

The authors declare no conflict of interest.

Data Availability Statement

The data that support the findings of this study are available from the corresponding author upon reasonable request.

Keywords

granular hydrogel, nanocomposite-modified electrode, non-invasive and continuous monitoring, sweat sampling at rest, wearable lactate sensor

Received: February 28, 2025
Revised: May 11, 2025
Published online:

[1] A. Koh, D. Kang, Y. Xue, S. Lee, R. M. Pielak, J. Kim, T. Hwang, S. Min, A. Banks, P. Bastien, *Sci. Transl. Med.* **2016**, *8*, 366ra165.
[2] W. Gao, S. Emaminejad, H. Y. Y. Nyein, S. Challa, K. Chen, A. Peck, H. M. Fahad, H. Ota, H. Shiraki, D. Kiriya, *Nature* **2016**, *529*, 509.
[3] J. Heikenfeld, *Nature* **2016**, *529*, 475.
[4] M. Bariya, H. Y. Y. Nyein, A. Javey, *Nat. Electron.* **2018**, *1*, 160.
[5] Y. Yu, H. Y. Y. Nyein, W. Gao, A. Javey, *Adv. Mater.* **2020**, *32*, 1902083.
[6] V. Mani, T. Beduk, W. Khushaim, A. E. Ceylan, S. Timur, O. S. Wolfbeis, K. N. Salama, *TrAC Trends Anal. Chem.* **2021**, *135*, 116164.
[7] Y. Ye, Y. Ge, Q. Zhang, M. Yuan, Y. Cai, K. Li, Y. Li, R. Xie, C. Xu, D. Jiang, *Adv. Sci.* **2022**, *9*, 2104738.
[8] W.-C. Tai, Y.-C. Chang, D. Chou, L.-M. Fu, *Biosensors* **2021**, *11*, 260.
[9] Z. Sonner, E. Wilder, J. Heikenfeld, G. Kasting, F. Beyette, D. Swaile, F. Sherman, J. Joyce, J. Hagen, N. Kelley-Loughnane, *Biomicrofluidics* **2015**, *9*, 31301.
[10] L. B. Baker, *Temperature* **2019**, *6*, 211.
[11] A. Hauke, P. Simmers, Y. R. Ojha, B. D. Cameron, R. Ballweg, T. Zhang, N. Twine, M. Brothers, E. Gomez, J. Heikenfeld, *Lab Chip* **2018**, *18*, 3750.
[12] S. M. Khor, J. Choi, P. Won, S. H. Ko, *Nanomaterials* **2022**, *12*, 221.
[13] O. Parlak, S. T. Keene, A. Marais, V. F. Curto, A. Salleo, *Sci. Adv.* **2018**, *4*, aar2904.
[14] M. A. Yokus, T. Songkakul, V. A. Pozdin, A. Bozkurt, M. A. Daniele, *Biosens. Bioelectron.* **2020**, *153*, 112038.
[15] W. Jia, A. J. Bandodkar, G. Valdés-Ramírez, J. R. Windmiller, Z. Yang, J. Ramírez, G. Chan, J. Wang, *Anal. Chem.* **2013**, *85*, 6553.
[16] H. Y. Y. Nyein, M. Bariya, L. Kivimäki, S. Uusitalo, T. S. Liaw, E. Jansson, C. H. Ahn, J. A. Hangasky, J. Zhao, Y. Lin, *Sci. Adv.* **2019**, *5*, aaw9906.
[17] A. Alizadeh, A. Burns, R. Lenigk, R. Gettings, J. Ashe, A. Porter, M. McCaul, R. Barrett, D. Diamond, P. White, *Lab Chip* **2018**, *18*, 2632.
[18] S. Li, Z. Ma, Z. Cao, L. Pan, Y. Shi, *Small* **2020**, *16*, 1903822.
[19] S. Wang, M. Liu, X. Yang, Q. Lu, Z. Xiong, L. Li, H. Zheng, S. Feng, T. Zhang, *Biosens. Bioelectron.* **2022**, *210*, 114351.
[20] J. T. Reeder, J. Choi, Y. Xue, P. Gutruf, J. Hanson, M. Liu, T. Ray, A. J. Bandodkar, R. Avila, W. Xia, *Sci. Adv.* **2019**, *5*, aau6356.
[21] C. B. Goy, R. E. Chaile, R. E. Madrid, *React. Funct. Polym.* **2019**, *145*, 104314.
[22] J. Nie, J. Fu, Y. He, *Small* **2020**, *16*, 2003797.
[23] D. J. Beebe, J. S. Moore, Q. Yu, R. H. Liu, M. L. Kraft, B.-H. Jo, C. Devadoss, *Proc. Natl. Acad. Sci.* **2000**, *97*, 13488.
[24] H. Zhao, X. Zhang, Y. Qin, Y. Xia, X. Xu, X. Sun, D. Yu, S. M. Mugo, D. Wang, Q. Zhang, *Adv. Funct. Mater.* **2023**, *33*, 2212083.
[25] P.-H. Lin, S.-C. Sheu, C.-W. Chen, S.-C. Huang, B.-R. Li, *Talanta* **2022**, *241*, 123187.
[26] T. Shay, M. D. Dickey, O. D. Velev, *Lab Chip* **2017**, *17*, 710.
[27] S. H. D. Wong, G. R. Deen, J. S. Bates, C. Maiti, C. Y. K. Lam, A. Pachauri, R. AlAnsari, P. Bělský, J. Yoon, J. M. Dodda, *Adv. Funct. Mater.* **2023**, *33*, 2213560.
[28] T. W. Shay, in *Hydrogel and Microfluidic Enabling Technologies for Wearable Biomonitoring Devices: Sweat and ECG Sensing*, North Carolina State University, Raleigh, NC, USA **2017**.
[29] H. Yu, J. Sun, *Nanotechnol. Precis. Eng.* **2020**, *3*, 126.
[30] T. Saha, J. Fang, S. Mukherjee, C. T. Knisely, M. D. Dickey, O. D. Velev, *Micromachines* **2021**, *12*, 1513.
[31] T. Saha, J. Fang, M. A. Yokus, S. Mukherjee, A. Bozkurt, M. A. Daniele, M. D. Dickey, O. D. Velev, presented at 2021 43rd Annual Int. Conf. of the IEEE Engineering in Medical & Biology Society (EMBC), Mexico, November **2021**, pp. 6863–6866.
[32] H. Shafique, J. de Vries, J. Strauss, A. Khorrami Jahromi, R. Siavash Moakhar, S. Mahshid, *Adv. Healthcare Mater.* **2023**, *12*, 2201501.
[33] P. Bacchin, J. Leng, J.-B. Salmon, *Chem. Rev.* **2021**, *122*, 6938.
[34] A. Herrmann, R. Haag, U. Schedler, *Adv. Healthcare Mater.* **2021**, *10*, 2100062.
[35] V. F. Curto, S. Coyle, R. Byrne, N. Angelov, D. Diamond, F. Benito-Lopez, *Sensors Actuat., B Chem.* **2012**, *175*, 263.
[36] T. Saha, S. Mukherjee, M. D. Dickey, O. D. Velev, *Lab Chip* **2024**, *24*, 1244.
[37] T. Saha, J. Fang, S. Mukherjee, M. D. Dickey, O. D. Velev, *ACS Appl. Mater. Interfaces* **2021**, *13*, 8071.
[38] H. Y. Y. Nyein, M. Bariya, B. Tran, C. H. Ahn, B. J. Brown, W. Ji, N. Davis, A. Javey, *Nat. Commun.* **2021**, *12*, 1823.
[39] I. Jeerapan, C. Moonla, P. Thavarungkul, P. Kanatharana, *Prog. Mol. Biol. Transl. Sci.* **2022**, *187*, 249.
[40] A. Sanati, Y. Esmaeili, E. Bidram, L. Shariati, M. Rafienia, S. Mahshid, O. Parlak, *Appl. Mater. Today* **2022**, *26*, 101350.
[41] G. Bolat, E. De la Paz, N. F. Azeredo, M. Kartolo, J. Kim, A. N. de Loyola e Silva, R. Rueda, C. Brown, L. Angnes, J. Wang, J. R. Sempionatto, *Anal. Bioanal. Chem.* **2022**, *414*, 5411.
[42] M. Ding, L. Jing, H. Yang, C. E. Machnicki, X. Fu, K. Li, I. Y. Wong, P.-Y. Chen, *Mater. Today Adv.* **2020**, *8*, 100088.
[43] R. A. Siegel, Y. Gu, M. Lei, A. Baldi, E. E. Nuxoll, B. Ziaie, *J. Controlled Release* **2010**, *141*, 303.
[44] N. Adly, S. Weidlich, S. Seyock, F. Brings, A. Yakushenko, A. Offenhäusser, B. Wolfrum, *npj Flex. Electron.* **2018**, *2*, 15.
[45] B. J. Kirby, in *Micro-and Nanoscale Fluid Mechanics: Transport in Microfluidic Devices*, Cambridge University Press, Cambridge, UK **2010**.
[46] R. Guo, X. Wang, W. Yu, J. Tang, J. Liu, *Sci. China Technol. Sci.* **2018**, *61*, 1031.
[47] J. Cai, T. Jin, J. Kou, S. Zou, J. Xiao, Q. Meng, *Langmuir* **2021**, *37*, 1623.
[48] Z. Ataie, S. Horchler, A. Jaberi, S. V Koduru, J. C. El-Mallah, M. Sun, S. Kheirabadi, A. Kedzierski, A. Risbud, A. R. A. E. Silva, *Small* **2023**, *20*, 2307928.
[49] T. H. Qazi, J. Wu, V. G. Muir, S. Weintraub, S. E. Gullbrand, D. Lee, D. Issadore, J. A. Burdick, *Adv. Mater.* **2022**, *34*, 2109194.
[50] A. Jaberi, A. Kedzierski, S. Kheirabadi, Y. Tagay, Z. Ataie, S. Zavari, M. Naghashnejad, O. Waldron, D. Adhikari, G. Lester, *Adv. Healthcare Mater.* **2024**, *13*, 2402489.
[51] T. R. Ray, J. Choi, A. J. Bandodkar, S. Krishnan, P. Gutruf, L. Tian, R. Ghaffari, J. A. Rogers, *Chem. Rev.* **2019**, *119*, 5461.
[52] T. Dodevska, Y. Lazarova, I. Shterev, *Acta Chim. Slov.* **2019**, *66*, 762.
[53] Á. Torrinha, C. G. Amorim, M. C. Montenegro, A. N. Araújo, *Talanta* **2018**, *190*, 235.
[54] G. Xiao, J. He, Y. Qiao, F. Wang, Q. Xia, X. Wang, L. Yu, Z. Lu, C.-M. Li, *Adv. Fiber Mater.* **2020**, *2*, 265.
[55] F. Gao, C. Liu, L. Zhang, T. Liu, Z. Wang, Z. Song, H. Cai, Z. Fang, J. Chen, J. Wang, *Microsyst. Nanoeng.* **2023**, *9*, 1.
[56] F. Lorestani, X. Zhang, A. M. Abdullah, X. Xin, Y. Liu, M. M. Rahman, M. A. S. Biswas, B. Li, A. Dutta, Z. Niu, *Adv. Funct. Mater.* **2023**, *33*, 2306117.
[57] J. Zhu, Y. Xiao, X. Zhang, Y. Tong, J. Li, K. Meng, Y. Zhang, J. Li, C. Xing, S. Zhang, *Adv. Mater.* **2024**, *36*, 2400236.
[58] N. M. Huang, H. N. Lim, C. H. Chia, M. A. Yarmo, M. R. Muhamad, *Int. J. Nanomed.* **2011**, *6*, 3443.
[59] Y. Mohd, R. Ibrahim, M. F. Zainal, presented at 2012 IEEE Symp. Humanities, Science and Engineering Research, Kuala Lumpur, Malaysia, June **2012**, pp. 1301–1306.

[60] A. Gökaltun, Y. B. (Abraham) Kang, M. L. Yarmush, O. B. Usta, A. Asatekin, *Sci. Rep.* **2019**, *9*, 7377.
[61] J. M. de Rutte, J. Koh, D. Di Carlo, *Adv. Funct. Mater.* **2019**, *29*, 1900071.
[62] K. Yue, X. Li, K. Schrobback, A. Sheikhi, N. Annabi, J. Leijten, W. Zhang, Y. S. Zhang, D. W. Hutmacher, T. J. Klein, *Biomaterials* **2017**, *139*, 163.
[63] Z. Ataie, S. Kheirabadi, J. W. Zhang, A. Kedzierski, C. Petrosky, R. Jiang, C. Vollberg, A. Sheikhi, *Small* **2022**, *18*, 2202390.
[64] Y. Muramoto, D. Nakashima, T. Amano, T. Harita, K. Sugai, K. Daigo, Y. Iwasawa, G. Ichihara, H. Okawara, T. Sawada, *Sci. Rep.* **2023**, *13*, 10366.
[65] P.-H. Lin, H.-H. Nien, B.-R. Li, *Annu. Rev. Anal. Chem.* **2023**, *16*, 181.
[66] H. Y. Y. Nyein, M. Bariya, B. Tran, C. H. Ahn, B. J. Brown, W. Ji, N. Davis, A. Javey, *Nat. Commun.* **2021**, *12*, 1823.
[67] H. Y. Y. Nyein, L.-C. Tai, Q. P. Ngo, M. Chao, G. B. Zhang, W. Gao, M. Bariya, J. Bullock, H. Kim, H. M. Fahad, *ACS Sens.* **2018**, *3*, 944.
[68] Y. Zheng, A. Wang, *Eur. Polym. J.* **2015**, *72*, 661.
[69] S.-G. Wang, X.-F. Sun, X.-W. Liu, W.-X. Gong, B.-Y. Gao, N. Bao, *Chem. Eng. J.* **2008**, *142*, 239.
[70] C. Xu, F. Wu, P. Yu, L. Mao, *ACS Sens.* **2019**, *4*, 3102.
[71] M. R. Romero, F. Garay, A. M. Baruzzi, *Sensors Actuat. B Chem.* **2008**, *131*, 590.
[72] Q. Chen, T. Sun, X. Song, Q. Ran, C. Yu, J. Yang, H. Feng, L. Yu, D. Wei, *Nanotechnology* **2017**, *28*, 315501.
[73] T. N. Huan, T. Ganesh, K. S. Kim, S. Kim, S.-H. Han, H. Chung, *Biosens. Bioelectron.* **2011**, *27*, 183.
[74] J. R. Whitaker, in *Handbook Food Enzymology*, CRC Press, Boca Raton, FL, USA **2002**, pp. 46–63.
[75] Y. Zhao, Y. Yu, S. Zhao, R. Zhu, J. Zhao, G. Cui, *Microchem. J.* **2023**, *185*, 108092.
[76] F. Mazzara, B. Patella, C. D'Agostino, M. G. Bruno, S. Carbone, F. Lopresti, G. Aiello, C. Torino, A. Vilasi, A. O'Riordan, *Chemosensors* **2021**, *9*, 169.
[77] J. Liao, X. Zhang, Z. Sun, H. Chen, J. Fu, H. Si, C. Ge, S. Lin, *Biosensors* **2022**, *12*, 397.
[78] G.-P. Nikoleli, C. G. Siontorou, D. P. Nikolelis, S. Bratakou, S. Karapetis, N. Tzamtzis, *Nanotechnol. Biosens.* **2018**, 375.
[79] J. S. Kuo, D. T. Chiu, *Annu. Rev. Anal. Chem.* **2011**, *4*, 275.
[80] J.-H. Han, S. H. Park, S. Kim, J. J. Pak, *Bioelectrochemistry* **2022**, *148*, 108259.
[81] C. J. Harvey, R. F. LeBouf, A. B. Stefaniak, *Toxicol. Vitr.* **2010**, *24*, 1790.
[82] M. Yu, Y.-T. Li, Y. Hu, L. Tang, F. Yang, W.-L. Lv, Z.-Y. Zhang, G.-J. Zhang, *J. Electroanal. Chem.* **2021**, *882*, 115029.
[83] A. Khan, M. Winder, G. Hossain, *Biosens. Bioelectron. X* **2022**, *10*, 100103.
[84] W. Heng, G. Yang, W. S. Kim, K. Xu, *Bio-Design Manuf.* **2021**, *5*, 64.
[85] T. Saha, T. Songkakul, C. T. Knisely, M. A. Yokus, M. A. Daniele, M. D. Dickey, A. Bozkurt, O. D. Velev, *ACS Sens.* **2022**, *7*, 2037.
[86] Y. Zhu, R. Haghniaz, M. C. Hartel, S. Guan, J. Bahari, Z. Li, A. Baidya, K. Cao, X. Gao, J. Li, *Adv. Mater.* **2023**, *35*, 2209300.